Nanoscale

PAPER

View Article Online
View Journal | View Issue

Cite this: *Nanoscale*, 2026, **18**, 4300

Gadolinium-assisted synthesis of Pt/C electrocatalysts: WAXTS–DSE insights into active area and ORR activity

Mattia Parnigotto, *[a] Gregorio Dal Sasso, [b] Marco Mazzucato, [a] Maria Chiara Dalconi, [c] Denis Badocco,[a] Enzo Menna, [a] Paolo Pastore, [a] Marzio Rancan,[d] Lidia Armelao[a] and Christian Durante *[a]

Received 3rd November 2025,
Accepted 20th January 2026

DOI: 10.1039/d5nr04642d

rsc.li/nanoscale

This paper reports on the template-assisted synthesis of Pt-based catalysts featuring a porous structure. The influence of various gadolinium precursors on the synthesis of Pt–Gd oxide catalysts is systematically investigated, with the objective of optimizing their crystalline structure and correlating it with their performance in the oxygen reduction reaction (ORR). Transmission electron microscopy analyses reveal complex morphological features, while synchrotron radiation experiments, combined with an innovative and robust approach based on the Debye Scattering Equation (DSE), enable a more accurate correlation between the electrochemical performance and the actual morphology of the catalysts. Although this work does not claim the development of a breakthrough catalyst, the observed ORR activity is comparable to that of commercial benchmarks (*e.g.*, TKK). More importantly, it underscores the value of DSE-based XRD analysis as a statistically rigorous and complementary technique for nanoparticle morphology characterization, offering significant advantages over conventional TEM in this context.

1 Introduction

Proton Exchange Membrane Fuel Cells (PEM-FCs) are efficient energy devices used in both portable and stationary systems. While PEM-FCs demonstrate high energy conversion efficiency, their widespread adoption is hindered by the high cost of the catalytic materials used.[1] Both the cathodic and anodic compartments of PEM-FCs require catalysts because the oxygen reduction reaction (ORR, $O_2 + 4H^+ + 4e^- \rightarrow 2H_2O$) and to a lesser extent Hydrogen Oxidation Reaction (HOR, $H_2 \rightarrow 2H^+ + 2e^-$) are kinetically slow processes.[2,3]

Platinum on carbon (Pt/C) catalysts are the most commonly used to accelerate the reaction rates of the ORR, but the reliance on platinum presents a significant barrier to the commercialization of PEM-FCs, as it accounts for approximately 70% of the total cost of the system.[4] Consequently, research efforts are focused on two main approaches to facilitate PEM-FC commercialization: (i) developing new catalysts based on non-platinum group metals (non-PGM), such as iron–nitrogen single-site catalysts,[5–7] cobalt, and nickel materials;[8–12] or (ii) improving the electrochemical performance of platinum-based catalysts.[13] The goal of the latter approach is to reduce the amount of platinum needed while maintaining catalytic activity, thereby lowering costs.

The catalytic performance of platinum can be enhanced through what are known as the "ligand effect" and the "geometric effect".[14] These effects are induced by incorporating a second element such as gadolinium, yttrium, scandium, nickel, iron, or cobalt into the platinum crystal structure. The ligand effect involves a change in the electronic configuration of the platinum due to its interaction with the added transition or rare-earth element. The geometric effect, on the other hand, refers to the alteration of the interatomic distances between platinum atoms on the surface, caused by differences in atomic size between platinum and the second element. These two effects adjust the orbital energy of the d-band of Pt, which in turn modifies the adsorption energy and thus its catalytic activity.[15–18]

According to literature, the bulk alloyed forms of Pt_5Gd and Pt_3Y are among the most stable face-centered cubic (fcc) alloys. Electrochemical studies on platinum–rare-earth alloys have demonstrated exceptionally high ORR activity and stability.[19–21] However, the synthesis of these alloys presents

[a]*Department of Chemical Sciences, University of Padova, Via Marzolo 1, 35131 Padova, Italy. E-mail: christian.durante@unipd.it*
[b]*Italian National Research Council, Institute of Geosciences and Earth Resources, Corso Stati Uniti 4, Padova 35127, Italy*
[c]*Department of Geosciences, University of Padova, Via Gradenigo 6, Padova 35131, Italy*
[d]*Institute of Condensed Matter Chemistry and Technologies for Energy (ICMATE), National Research Council (CNR), c/o Department of Chemistry, University of Padova, via F. Marzolo 1, 35131 Padova, Italy*

significant challenges, particularly due to the slow reduction of Y^{3+} and Gd^{3+} to their metallic forms (Y^0 and Gd^0), as indicated by their standard reduction potentials. This makes the production of Pt_5Gd and Pt_3Y particularly difficult.[22]

Attempts to synthesize Pt_xY/C alloy nanoparticles *via* a simple, low-cost chemical reduction method using $NaBH_4$, followed by thermal treatment at 350 °C, have resulted only in the formation of PtY_2O_3 nanoparticles (NPs) rather than the desired metallic alloy.[23] The most effective methods for synthesizing platinum–yttrium metallic alloys, such as (co-)sputtering deposition in an ultra-high vacuum (UHV) chamber, are based on metallurgical techniques. However, these methods are both expensive and difficult to implement in a standard chemical laboratory setting. Similarly, the synthesis of Pt_5Gd involves complex, costly procedures that are unsuitable for scalable production. As a result, even if some promising synthetic strategies were proposed in the literature,[13,24] researchers have shifted focus toward the synthesis of platinum-metal oxide (Pt-MO_x) catalysts.[25–27] Numerous studies in the literature report that PtY_2O_3/C catalysts exhibit specific and mass activities that are 1.3 and 1.6 times higher, respectively, than those achieved with commercial Pt/C catalysts.[28,29] A similar trend is observed with gadolinium-based catalysts; for example, $PtGd_2O_3$/carbon with a 25 wt% platinum loading has demonstrated performance comparable to that of Pt/C TKK catalysts with 50 wt% platinum content.[29]

A recent study investigated a series of Pt_xGd/C nanostructured electrocatalysts synthesized *via* the carbodiimide complex route, where the Pt/Gd ratio was systematically varied. The findings revealed that the Pt/Gd ratio significantly influences the crystalline structure, particle size, near-surface chemistry, and consequently, the electrochemical performance towards the ORR.[24]

Herein, we aim to explore the correlation between different gadolinium precursors ($GdCl_3$, Gd-acetylacetonate, and Gd-acetate), synthesis temperatures, and ORR performance when utilizing a solid-state synthesis approach. Notably, in the synthesized Pt–Gd materials, gadolinium predominantly exists in its oxide form. Subsequent acid leaching removes residual gadolinium, which initially served as a template influencing the morphology and dimensions of the platinum nanoparticles. Different gadolinium precursors result in varying nanoparticle sizes and shapes, with Gd-acetylacetonate proving most effective in promoting optimal Pt nanoparticle growth during synthesis. This process ultimately yields a catalyst with enhanced performance. To thoroughly investigate the relationship between the synthesis parameters and ORR activity, we employed synchrotron wide-angle X-ray total scattering (WAXTS) experiments, coupled with advanced data analysis using the Debye Scattering Equation (DSE).[30,31] This method allowed us to examine the correlation between the specific surface area (SSA) and ORR performance in detail, as also shown in a related study.[32] These findings underscore the power of X-ray total scattering techniques when used to correlate catalytic performance with the properties of complex composite materials exhibiting inhomogeneous dispersion.

2 Materials and methods

2.1 Chemicals

Vulcan XC72 (C) (Fuel Cell Store), Pt(II) acetylacetonate (Sigma Aldrich, >99.9%), Nafion® (Sigma Aldrich, 5 wt% in EtOH), Gd (III) acetylacetonate hydrate (Sigma Aldrich, >99.9%), Gd(III) acetate hydrate (Sigma Aldrich, 99.9%), Gd(III) chloride hexahydrate (Sigma Aldrich, >99%), $HClO_4$ (Fluka, Traceselect® 67–72%), H_2SO_4 (Fluka, Traceselect® >95%), NOCHROMIX®, (Sigma Aldrich-Glass-Cleaning Reagent), Pt/C Tanaka standard (TEC10V50E), and acetone (Fluka, HPLC grade) were used as received without further purification. Alpha Gaz O_2 and Argon were supplied by Air Liquid at the highest available purity (>99.99%).

2.2 Instrumentation

X-ray photoelectron spectroscopy (XPS) measurements were performed with a Thermo Scientific ESCALAB QXi spectrometer employing a monochromatic AlKα X-ray source (1486.6 eV) with a spot size of 650 μm × 200 μm *circa*. Survey scans were measured in a binding energy range of 0–1350 eV with a constant pass energy of 100 eV, at 1.0 eV per step, with a dwell time of 50 ms. High resolution spectra were recorded using a constant pass energy (20 eV), at 0.1 eV per step, with a dwell time of 50 ms. Peak fittings were performed in the framework of the Avantage software after background correction with the smart-background function implemented in the same software using pseudo-Voigt functions for the synthetic peaks. The Pt 4f spectrum of a sputter-cleaned Pt(111) sample was used to determine the fitting parameters for the metallic contribution (FWHM = 0.79 eV, L/G mix product 76.6%, tail mix 61.98%, tai height 0.13%, tail exponent 0.0334). The Pt 4f peak was fitted according to the parameters of Table S2. For Gd 4d photoemission peak, the ^{9}D component was deconvoluted using the fitting parameters (intensity and energy separation, Table S3) derived for pure Gd metal by Gupta and coworkers.[33]

Thermogravimetric analysis (TGA) was performed using a Q5000IR (TAWaters) on 3 mg samples at a heating rate of 10 °C min^{-1} from 100 °C to 1000 °C in a N_2 environment to determine the thermal stability. Transmission electron microscopy (TEM) images were obtained by using a FEI Tecnai G2 transmission electron microscope operating at 100 kV. Inductively coupled plasma mass spectrometry analysis (ICP-MS) for the determination of the Pt content was carried out with an Agilent Technologies 7700x ICP-MS (Agilent Technologies International Japan, Ltd, Tokyo, Japan). A Microwave Digestion System (CEM EXPLORER SP-D PLUS) was used for the acid digestion. The ICP-MS instrument was equipped with an octopole collision cell operating in kinetic energy discrimination mode used for the removal of polyatomic interferences and argon-based interferences.

2.3 Catalysts synthesis

$PtGdO_x$ NPs@C were synthetized by solid-state synthesis at high temperatures in a reducing atmosphere.[22,34] $Pt(acac)_2$ is the fastest reduction platinum precursor, it shows a very low

decomposition temperature.[22] $Pt(acac)_2$ and Gd precursors were dispersed in ethanol and stirred until the complete dissolution, after carbon was added to the solution to obtain a final Pt(0) loading of 30%. Generally, in a typical synthesis 35.5 mg of $Pt(acac)_2$ was mixed with *ca.* 10 mg of Gd precursor and 46 mg of carbon in 15 mL of ethanol. The precursor solution was sonicated at room temperature for 2 h, and after dried for 12 h at 80 °C. The precursor powder was, also, ground in an agate mortar to obtain a very good distribution and mixing and transferred in a quartz boat for the synthesis. The $PtGdO_x$ precursor powder was treated in a tubular furnace (Carbolite, UK) at high temperature under a H_2/N_2 combined atmosphere with a flow of 2 sccm and 28 sccm, respectively. Before starting the heat treatment, the furnace was purged by fluxing only N_2 (using a flow of 30 sccm) for 1 h at room temperature (r.t.). Then the temperature increased until 100 °C and was kept constant for 1 h, at the same time, H_2 was gradually fluxed into the quartz tube to the desired ratio (2 sccm), and the N_2 flow was decreased at 28 sccm. This step is crucial for the complete desorption of water and oxygen species from the powder precursors. Then, the temperature was allowed to increase to the temperature synthesis and kept constant for 5 h. Eventually, the furnace was allowed to cool down to r.t., while the H_2 flow was switched off, allowing only N_2 to flow inside the reactor.

The catalysts were transferred to a double-necked flask containing 100 mL of H_2SO_4 1 M solution. The resulting solution was stirred for 1 h at room temperature. Afterwards, the catalyst was filtered with a nylon nanometric filter (GVS, nylon 0.2 μm, 47 mm membrane diameter) and carefully washed with 500 mL of ultra-pure water. Finally, drying in an oven at 80 °C overnight.[35]

2.4 Electrochemical set-up and characterization

Cyclic Voltammetries (CVs) and Linear Sweep Voltammetries (LSVs) with Rotating Disk Electrode (RDE) were recorded in 0.1 M $HClO_4$ in a classic three-electrode cell at 25 °C by using a Biologic SP-300 potentiostat/galvanostat. An RDE with a glassy carbon (GC, 5 mm diameter tip, geometric surface area 0.196 cm^2, Biologic) and a Pt ring (Amel instruments for Electrochemistry) were used as working (WE) and counter electrode (CE), respectively. GCs were preliminarily polished using diamond pastes (3 μm, 1 μm, and 0.25 μm). The reference electrode, to which all reported potentials are referred, was an RHE, which was prepared before each electrochemical characterization. The $PtGdO_x$ catalysts were characterized as thin film drop casted on the GC-RDE. The ink was drop casted using a platinum loading of 15 μg cm^{-2}. The ink was formulated for drop casted *ca.* 12–15 μL on the GC RDE, in a typical experiment 1.25 mg of $PtGdO_x$@C catalysts, 0.1 mL of isopropanol, 1.1 mL of water and 3 μL of Nafion® was mixed for 30 minutes and sonicated for 3 h, after the ink was drop casted in the GC electrode surface and allowed to dry under rotation at 500 rpm at room temperature. The $HClO_4$ electrolyte solution was purged with Ar before each measurement, whereas for the ORR test, the electrolyte was bubbled with high-purity Oxygen for at least 30 min to ensure O_2 saturation.[36,37]

The $PtGdO_x$@C catalysts were first electrochemically activated by performing 100 voltammetric cycles at 50 mV s^{-1} between 0.05 V and 1.2 V *vs.* RHE or until stable cyclic voltammograms (CVs) were obtained. The ORR activity was determined by recording Linear Sweep Voltammograms (LSVs) at a scan rate of 20 mV s^{-1} and a rotation rate of 1600 rpm between 0.05 V *vs.* RHE and 1.1 V *vs.* RHE, in O_2-saturated electrolyte. To analyze only the ORR current, the LSV with RDE polarization curves were corrected by subtracting background surface oxidation and capacitive processes. This involves subtraction of the background CV recorded in the Argon saturated electrolyte (obtained using the same experimental parameters, *i.e.*, scan speed, rotation rate, potential window) from the ORR polarization curves; in all the electrochemical analysis the IR drop was compensated by positive feedback. The electrochemical area (ECA) was calculated by the coulometry of the hydrogen under-potential deposition (H_{upd}), using a charge of 210 μC cm^{-2} using the CV recorded in Argon saturated electrolyte solution at different scan rate. The CVs in Argon saturated electrolyte were recorded in the range 0.00–1.00 V *vs.* RHE using a scan rate of 50 mV s^{-1}. The ORR activity was evaluated using the kinetic current calculated using the LSV with RDE at 20 mV s^{-1} and 1600 rpm.[36,38] The ECA was calculated using the following formula:

$$\mathrm{ECA} = \frac{Q_{\mathrm{upd}}}{q \times m_{\mathrm{Pt}}} \quad (1)$$

The kinetic current density j_k was determined using a rotating electrode rotated at 1600 rpm. The current density was taken at 0.9 V *versus* RHE[39] and corrected by mass transfer, according to

$$j_k = \frac{j_{\mathrm{lim}} \times j_{0.9\mathrm{V}\,vs.\,\mathrm{RHE}}}{j_{\mathrm{lim}} - j_{0.9\mathrm{V}\,vs.\,\mathrm{RHE}}} \quad (2)$$

The catalyst activity was evaluated considering the mass activity and the specific activity obtained through the following equation:

$$\mathrm{MA} = \frac{j_k}{m_{\mathrm{Pt}}} \quad (3)$$

$$\mathrm{SA} = \frac{j_k}{\mathrm{ECA} \times m_{\mathrm{Pt}}} \quad (4)$$

The statistical errors associated with the electrochemical parameters were determined from the standard deviation computed on nine independent values and/or by error propagation.

2.5 WAXTS measurements

WAXTS measurements were performed at the X04SA-MS beamline of the Swiss Light Source (Paul Scherrer Institut, Villigen, CH).[40] The beam energy was set at 22 keV; operational wavelength λ = 0.563291 Å was determined by measuring the silicon powder standard sample NIST 640c. Samples were loaded in a 0.3 mm diameter glass capillary and WAXTS data were collected in transmission mode in the 0.07–19 $Å^{-1}$ Q

range (where $Q = 4\pi \sin\theta/\lambda$, 2θ is the scattering angle), using a single-photon counting silicon microstrip MYTHEN III detector. A separate measurement of the Vulcan XC 72 was performed. The transmission coefficient of the samples was experimentally determined by measuring the direct and transmitted beams, whereas that of the glass capillary was calculated from the certified composition and wall thickness of the capillary. Separate air and empty capillary scattering measurements were collected. Raw data were corrected for systematic errors and absorption effects; the extra-sample contributions to the scattering pattern, *i.e.* the scattering from the capillary and the sample environment, were subtracted. The reduced WAXTS data containing only the sample scattering pattern were analyzed through the total scattering approach based on the Debye scattering equation (DSE). DSE-based refinements were performed in the 2–19 $Å^{-1}$ Q range.

2.6 The Debye scattering equation (DSE) method

The Debye scattering equation[30,31,41] enables the computation of the total X-ray scattering pattern in the reciprocal space of randomly oriented NPs from the distribution of interatomic distances within atomistic models. The simulated scattering pattern is calculated as:

$$I(Q) = \sum_{j=1}^{N} f_j(Q)^2 o_j + 2\sum_{j>i=1}^{N} f_j(Q) f_i(Q) T_j(Q) T_i(Q) o_j o_i \frac{\sin(Qd_{ij})}{(Qd_{ij})} \quad (5)$$

where $Q = 4\pi \sin\theta/\lambda$ is the magnitude of the scattering vector, λ is the radiation wavelength, f_j is the X-ray atomic form factor of atom j, d_{ij} is the interatomic distance between atom i and j, and N is the number of atoms in the NPs. T and o parameters refer to the thermal atomic displacement and site occupancy, respectively. The first summation accounts for the contribution of the zero distances of each atom from itself, whereas the second summation accounts for the non-zero distances between pairs of distinct atoms. The DSE modeling is carried through a bottom-up approach within the DebUsSy Suite.[31,42] Populations of atomistic models of nanocrystals of spherical shape at increasing size are generated according to one (Diameter) growth direction. Gaussian sampled interatomic distances and pseudomultiplicities are encoded in databases used to simulate the scattering pattern through the DSE.[43] The calculated scattering pattern is generated by the weighted sum of the patterns from each atomistic model according to their number fraction within a lognormal size distribution law. The calculated pattern is refined against the experimental one minimizing the difference using a simplex algorithm and refining a number of adjustable structural and microstructural parameters in the model. The number-based average size and size dispersion of a lognormal distribution function are optimized. The isotropic atomic thermal displacement (Debye–Waller B factor) is also refined. The goodness of fit (GoF, the square root of reduced χ^2) is the statistical descriptor used to evaluate the agreement between calculated and experimental patterns. The WAXTS pattern of the Vulcan-XC72 was separately measured and added as an additional phase in the DSE analysis and used as background, accounting for the X-ray scattering of the carbon support within the analyzed samples.

2.7 The atomic pair distribution function method

PDF represents another approach to the analysis of X-ray total scattering data, providing the probability of finding pairs of atoms separated by a distance r in real space.[44] This method is particularly suited to investigate the short-range order of amorphous and nanostructured materials, extracting structural information without any assumption on periodicity. Difference PDF is here applied to the amorphous-like trace that has been added as a background (together with the WAXTS pattern of the Vulcan-XC 72) during the DSE refinement, compensating the difference between the calculated and experimental patterns and modeled through a polynomial function. The analyzed trace was calculated in the reciprocal space as the difference between the total background and the WAXTS signal of the carbon support. The total scattering structure function $S(Q)$ was calculated using PDFgetX3,[45] then the atomic PDF is obtained through the sine Fourier transform of the reduced total scattering structure function $F(Q) = Q[S(Q) - 1]$ as:

$$G(r) = \frac{2}{\pi}\int_{Q_{\min}}^{Q_{\max}} Q[S(Q) - 1]\sin(Q_r)\mathrm{d}Q \quad (6)$$

where $Q = 4\pi \sin\theta/\lambda$ is the magnitude of the scattering vector. $Q_{\min}$ = 1.9 $Å^{-1}$ was set equal to that used for the DSE analysis and $Q_{\max}$ = 18.0 $Å^{-1}$ was determined by the experimental setup. Despite the experimental setup is not specifically tailored for PDF data acquisition (instead it is optimized for the DSE approach) and the $Q_{\max}$ value is slightly lower than that obtained from proper PDF experiments, the main structural correlations within the material can be reliably extracted.[46]

3 Results and discussion

3.1 TGA as guidance for the synthesis temperatures

$PtGdO_x$ NPs were synthesized *via* solid-state reduction using a tubular furnace. The precursor, $Pt(acac)_2$, was combined with commercial Carbon Black (Vulcan XC72) and three different gadolinium sources: $GdCl_3{\cdot}6H_2O$ ($PtGdO_x1$-T), $Gd(acac)_3{\cdot}H_2O$ ($PtGdO_x2$-T) and $Gd(ac)_3{\cdot}xH_2O$ ($PtGdO_x3$-T), where T indicates the synthesis temperature (acac = acetylacetonate, ac = acetate). The synthesis was conducted at different temperatures for 5 hours in an H_2/N_2 atmosphere (6.7% of H_2), where hydrogen acted as the reducing agent. The chosen temperatures were based on the degradation temperatures (T_{deg}) of the gadolinium precursors determined *via* thermogravimetric analysis, as shown in Fig. 1.[47]

A common feature across all TGA profiles is a distinct peak near 100 °C, more pronounced in the hydrated gadolinium precursors compared to the anhydrous $Pt(acac)_2$. This peak corresponds to the release of water molecules. Regarding the Pt catalyst precursor, its mass decreases significantly between 150 °C and 250 °C, consistent with the literature,[48,49] thus

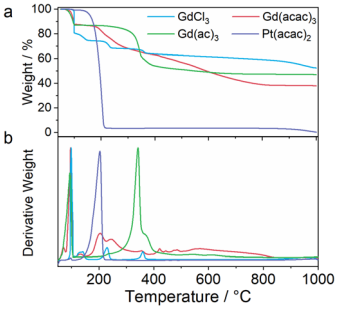

Fig. 1 Thermogravimetric analysis for the Gadolinium salt precursors, $GdCl_3$ blue line, $Gd(acac)_3$ red line and $Gd(ac)_3$ green line and for the Pt $(acac)_2$ purple line. For simplicity, the water molecules are not indicated in the legend nomenclature. The decomposition process was evaluated for (a) weight *vs.* temperature and (b) derivative weight *vs.* temperature.

excluding the decomposition of the Pt as a critical factor for the synthesis. However, the presence of water in the hydrated molecules may influence the reactions occurring at temperatures above 100 °C.

For instance, $GdCl_3{\cdot}6H_2O$ exhibits two distinct stages of water loss between 25 °C and 200 °C (blue line in Fig. 1), as described in the following reactions:[50]

$$GdCl_3 \cdot 6H_2O \rightarrow GdCl_3 \cdot 3H_2O + 3H_2O \uparrow \quad (7)$$

$$GdCl_3 \cdot 3H_2O \rightarrow GdCl_3 \cdot 2H_2O + H_2O \uparrow \quad (8)$$

$$GdCl_3 \cdot 2H_2O \rightarrow GdCl_3 \cdot H_2O + H_2O \uparrow \quad (9)$$

At higher temperatures, between 200 °C and 275 °C, hydrolysis occurs, forming anhydrous gadolinium salts. This leads to the production of gadolinium oxychloride through the following intermediate steps:

$$GdCl_3 \cdot H_2O \rightarrow GdCl_3 + H_2O \uparrow \quad (10)$$

$$GdCl_3 \cdot H_2O \rightarrow GdOCl + 2HCl \uparrow \quad (11)$$

A reaction peak between 300 °C and 400 °C corresponds to the dechlorination of residual anhydrous salts, resulting in the formation of GdOCl:

$$GdCl_3 \cdot 6H_2O \rightarrow GdOCl + 2HCl \uparrow + 5H_2O \uparrow \quad (12)$$

However, complete dechlorination occurs only at temperatures above 800 °C, according to literature.[51]

Temperatures above 600 °C were avoided to prevent damage to the carbon support, which degrades above this threshold.[52] Consequently, the synthesis temperatures were selected as 360 °C, to examine the temperature range associated with the dechlorination of the residual anhydrous salt, and 600 °C, the maximum applicable temperature, to evaluate its effects on particle size and catalytic activity while avoiding damage to the carbonaceous substrate.

For $Gd(ac)_3{\cdot}H_2O$, the green line in Fig. 1a shows the characteristic TGA profile,[53,54] where dehydration occurs at 100 °C. Additional decomposition mechanisms occur between 200 °C and 500 °C, with the final step involving the transformation:

$$(GdO)_2CO_3 \rightarrow Gd_2O_3 + CO_2 \uparrow \quad (13)$$

This suggests using 400 °C for synthesis to achieve the desired Pt-GdO_x material.

Finally, the complex decomposition behaviour of Gd $(acac)_3{\cdot}xH_2O$ (red line in Fig. 1) shows minor weight losses below 150 °C due to adsorbed and coordinated water. Multiple decomposition events, marked by two broad peaks in the derivative weight plot between 190 °C and 500 °C,[55] support selecting 500 °C as the optimal synthesis temperature for this precursor mixture. The different synthesis conditions are summarized in Table 1.

To address the potential presence of undesired species, such as Cl^- ions from $GdCl_3{\cdot}6H_2O$ precursor or other possible byproducts, an acid treatment was applied to the synthesized samples. This procedure was implemented based on literature recommendations, where similar composite materials were treated to remove contaminants.[24] The goal of the acid treatment was to eliminate residual chloride ions and any other impurities that may affect the performance or the stability of the composite catalysts including superficial Gd_2O_3. The treated samples were labelled by adding an "A" after the name of their untreated counterparts to indicate the acid treatment.

Both the treated and untreated samples were subjected to detailed electrochemical and morphological characterization.

3.2 Morphological characterization

Each sample was morphologically analysed using TEM characterization, revealing complex and notable features. For instance, the synthesis conducted with $GdCl_3$ resulted in a homogeneous dispersion of small metal NPs on the carbon support, with an average size ranging 3–15 nm. Additionally, some agglomerates were observed, reaching up to approximately 100 nm in diameter, as clearly shown in Fig. 2a and represented by the light blue bar in Fig. 2g. At lower temperatures, a similar dispersion with reduced agglomeration was achieved, as depicted in Fig. S1a and c.

When $Gd(acac)_3$ was used at 500 °C, the resulting nanoparticles displayed a comparable dispersion but without significant agglomeration (Fig. 2b and h). This observation suggests that the gadolinium ligand plays a distinct role in the synthesis process. Conversely, the catalyst synthesized with $Gd(ac)_3$ exhibited not only a broad size distribution but also very large agglomerates exceeding 100 μm, which were excluded from the dispersion analysis (Fig. 2c and i). Notably,

Table 1 Synthesis temperatures for PtGdO_xX catalysts synthesized using $Pt(acac)_2$ as Pt precursor

	Pt precursor	Gd precursor	Temperature (°C)
PtGdO_x1-*T*	$Pt(acac)_2$	$GdCl_3{\cdot}6H_2O$	360, 600
PtGdO_x2-*T*		$Gd(acac)_3{\cdot}xH_2O$	500
PtGdO_x3-*T*		$Gd(ac)_3{\cdot}xH_2O$	400

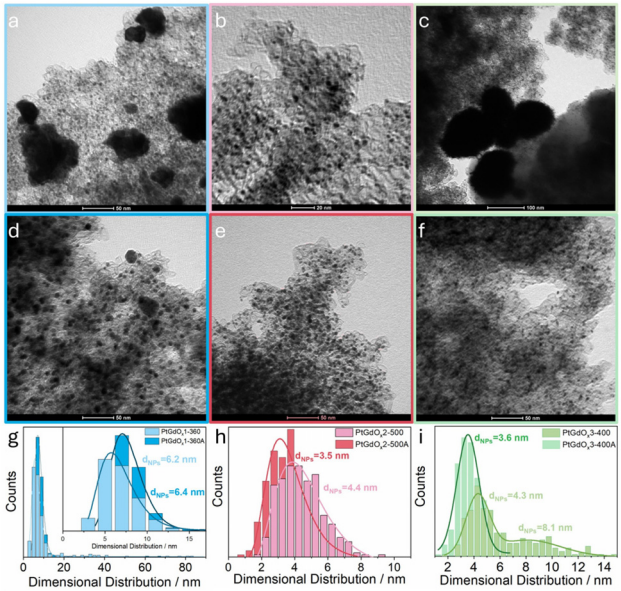

Fig. 2 TEM images for the pristine sample obtained at higher temperatures (a) $PtGdO_x$1-600; (b) $PtGdO_x$2-500; (c) $PtGdO_x$3-400; TEM images for the same samples after the acid treatment temperature (d) $PtGdO_x$1-600A; (e) $PtGdO_x$2-500A; (f) $PtGdO_x$3-400A; dimensional distribution for (g) $PtGdO_x$1-600; (h) $PtGdO_x$2-500; (i) $PtGdO_x$3–400 before (lighter color) and after the acid treatment (darker color).

this result was obtained despite the synthesis being conducted at one of the lowest temperatures, reinforcing the hypothesis that Gd precursors actively influence nanoparticle growth and agglomeration. These observations are consistent with previous reports, where the nature of the precursor or coordinating ligand was shown to strongly influence nucleation and growth phenomena. In particular, in solid-state reactions, specific ligands or precursors can confine metal species and suppress uncontrolled particle growth. For example, the thermal decomposition of the bimetallic compound [Fe(2,2′-bipyridine)$_3$][$PtCl_6$] on graphene oxide (GO) leads to homogeneously alloyed FePt nanocrystals, whereas in the absence of bipyridine ligands the individual Fe^{2+} and $PtCl_6^{2-}$ species cannot be effectively anchored, resulting in non-uniform metallic domains.[56] Likewise, metal oxide precursors such as cerium nitrate, when combined with Pt acetylacetonate, enhance metal–support interactions and act as a confinement medium, limiting Pt nanoparticle agglomeration and growth, as confirmed by *in situ* synchrotron diffraction coupled with DSE analysis. Collectively, our results align with these findings and further confirm that the chemical nature of Gd precursors plays a decisive role in dictating nanoparticle nucleation, growth, and agglomeration behavior.[57]

To enhance nanoparticle activity, as supported by prior research,[32] the samples were treated with sulfuric acid to remove potentially inactive oxide species and expose active sites. This treatment leads to a significant reduction in NP size across all samples, as shown in Fig. 2d–f, with sharper size distributions illustrated in Fig. 2g–i for $PtGdO_x$1-600, $PtGdO_x$2-500, and $PtGdO_x$1-400, respectively. An exception was observed for $PtGdO_x$1-360, where the nanoparticle dimensions remained unchanged (Fig. S1b and c). The acid treatment leads to less homogeneous structures, which are associated with improved electrocatalytic performance relative to the untreated samples. In light of that, a more statistical and complementary characterisation was carried out using DSE analysis.

3.3 Synchrotron WAXTS measurements and DSE analysis

WAXTS measurements were performed on the acid-treated samples ($PtGdO_x$1-600A, $PtGdO_x$2-500A, $PtGdO_x$3-400A) to achieve a detailed characterization of Pt NPs in terms of structure, morphology, and size. WAXTS data were analysed through the Debye Scattering Equation (DSE) method, according to a recently developed modelling approach for Pt NPs on carbon supports.[32,46,57] The experimental WAXTS pattern of the Vulcan XC72, separately measured, was added as a model component and scaled to the total scattering pattern of the catalysts, together with the DSE modelling of the Pt NPs. The latter is computed through the DSE from a population of atomistic models of isotropically shaped Pt NPs generated using a spherical model at increasing size according to one growth direction (diameter D), with a diameter step size of 0.3 nm. The Pt FCC unit cell, with cell parameter a = 3.9235 Å, was used as a building block for NP construction. The computed WAXTS pattern was optimized, against the experimental one, by refining the lattice parameters, the average size (D), and size dispersion (σD), according to a lognormal distribution law, and the isotropic atomic displacement parameters (Fig. 3). The WAXTS traces of samples $PtGdO_x$1-600A and $PtGdO_x$3-400A show a peculiar peak shape for the Pt phase, consisting of relatively sharp peaks and pronounced peak tails, typical of a population of NPs largely polydispersed in size.

The DSE computation of one single population of Pt NPs with a lognormal size distribution law, even though largely polydispersed, could not account for the experimental features. Therefore, a bimodal size distribution was required to account for such size dispersion, and it has been modelled by introducing a second population of Pt NPs as a model component, with refinable average size and size dispersion (using a lognormal distribution). Refined size and size dispersion for samples $PtGdO_x$1-600A and $PtGdO_x$3-400A highlight the occurrence of a large fraction of small NPs (<5 nm) and long tails of lognormally distributed populations of NPs accounting for few larger particles, whose mass is not negligible despite the low-frequency distribution (Fig. 3, Table 2). The relative mass fraction of the two populations of Pt NPs was also refined.

The need to introduce a secondary population to describe the WAXTS profile arises from the observation that, following acid leaching, not all large nanoparticles exhibited the expected size reduction as indicated by TEM analysis. This discrepancy underscores the value of WAXTS, which enables a more statistically robust assessment of particle size. Unlike TEM, which can provide a limited and potentially unrepresentative view of size and morphology, WAXTS offers a more com-

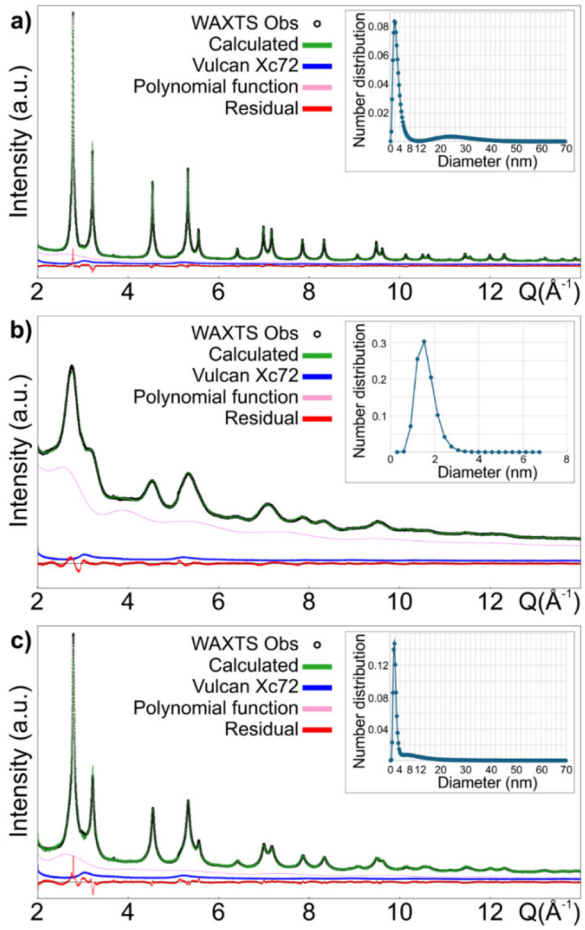

Fig. 3 WAXTS data (black) of PtGdO$_x$1-600A (a), PtGdO$_x$2-500A (b), and PtGdO$_x$3-400A (c) samples and best DSE fit (green); WAXTS traces of the Vulcan XC72 and the polynomial function used as model components in the WAXTS-DSE analysis are also displayed. Inset: Pt NPs size distribution derived from the DSE analysis.

prehensive characterization. Furthermore, the use of DSE enhances this capability by enabling the analysis of complex, multi-phase samples.

As observed in previous case studies,[32,46,57] all the samples show a significant amount of diffuse scattering that is not accounted for by model components, evidenced by a very broad, amorphous-like feature contributing to the whole scattering pattern.

Such a contribution was modelled by adding a polynomial function as a background component to the model and scaled to the WAXTS experimental patterns together with the experimental trace of the Vulcan XC72 and those of the computed DSE signal of 1 (PtGdO$_x$2-500A) or 2 (PtGdO$_x$1-600A, PtGdO$_x$3-400A) populations of Pt NPs. The Atomic Pair Distribution Function analysis of the polynomial function (Fig. S3) was calculated to investigate the nature of the scattering component.[44] The $G(r)$ curves show a peak at ~2.76 Å, compatible with the shortest Pt–Pt distance in metallic clusters, suggesting the possible occurrence of sub-nanometer Pt clusters within the samples,[58] contributing to the X-ray scattering pattern described through the polynomial function, as also observed in recently published articles.[32,46,57] Additionally, considering that the polynomial function is not optimized for a difference PDF analysis, we cannot rule out the possible contribution to the diffuse scattering of Pt oxides (possibly at the surface of Pt NPs), considering the non-negligible concentration of Pt oxidation states revealed by XPS analysis (Table S1). This contribution could be tentatively evidenced by modulations observed in the PDF signals at 1.9–2.3 Å and 3.2–3.5 Å, compatible with Pt–O bond length and Pt–Pt first distances in Pt oxide structures.[59]

Results on the number- and mass-based size distribution of Pt NPs were used to calculate the total specific surface area of the Pt NPs populations weighted for their relative mass fraction, neglecting aggregation effects between NPs. SSA has been shown to be particularly relevant as a descriptive parameter that can be effectively compared to the specific activity of the sample,[32,57] as shown in the next paragraph. Results of the DSE analysis of WAXTS data are collectively reported in Table 2.

3.4 XPS analyses and characterization

XPS analyses were performed on both treated and untreated samples synthesized at the highest temperatures, to investigate the chemical states of Pt and Gd, as well as the overall surface composition. Fig. 4a presents the survey spectra of the most relevant catalysts, showing characteristic photoemission peaks for Pt 4f, Gd 4d, C 1s, and O 1s. It is evident that acid-treated samples do not evidence any Gadolinium signal (Fig. 4b). The Pt 4f photoemission region was deconvoluted into four distinct components (Fig. 4d and e and Figures S4d–i), with the Pt 4f$_{7/2}$ peaks located at 71.0–71.1 eV, 71.6–71.8 eV, 72.7–72.9 eV and

Table 2 Results from the DSE analysis of the WAXTS data of PtGdO$_x$1-600A, PtGdO$_x$2-500A, and PtGdO$_x$3-400A. Number-based average diameter (D) and size dispersion (σD) of spherical Pt NPs according to a lognormal distribution law. Relative mass fraction of the two Pt NPs populations (when used), specific surface area (SSA) of Pt NPs populations, and total specific surface area of the sample weighted for the relative mass fraction of Pt NPs populations. Refined cell parameters and goodness of fit (GoF) of the best DSE fit are also reported

	D (nm)	σD (nm)	Mass fraction %	SSA (m^2 g^{-1})	SSA$_{tot}$ (m^2 g^{-1})	Cell (Å)	GoF
PtGdO$_x$1-600A	2.9	1.6	78.9	57.2	46.9	3.9212	5.66
PtGdO$_x$1-600A	27.8	8.5	21.1	8.4		3.9224	
PtGdO$_x$2-500A	1.6	0.4	100		151.7	3.9215	2.54
PtGdO$_x$3-400A	2.0	0.7	72.4	111.5	84.2	3.9223	6.84
PtGdO$_x$3-400A	11.4	7.3	27.6	12.6		3.9214	

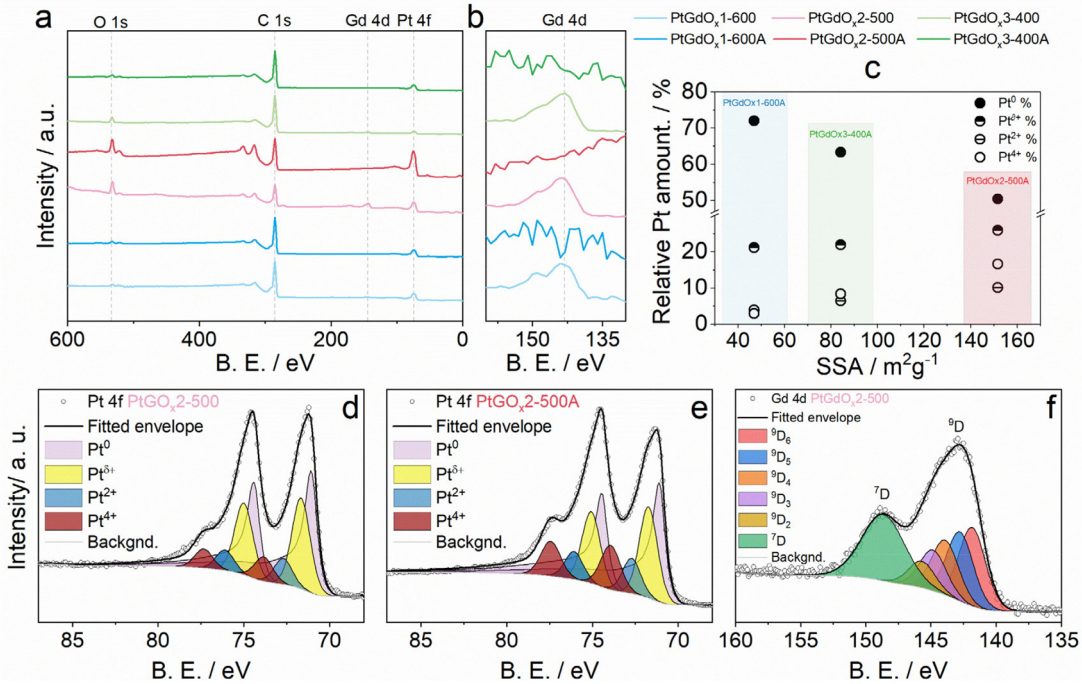

Fig. 4 (a) XPS surveys for the PtGdO$_x$ catalysts, (b) magnification of the Gd 4d photoemission region. (c) Relative Pt amount as derived from the fitting of the Pt 4f peak for samples PtGdO$_x$1-600A, PtGdO$_x$2-500A and PtGdO$_x$3-400A. Pt 4f region and deconvolution for (d) PtGdO$_x$2-500 and (e) PtGdO$_x$2-500A, (f) Gd 4d region and deconvolution for PtGdO$_x$2-500.

73.8–74.0 eV corresponding to Pt^0, Pt$^{\delta+}$, Pt^{2+}, and Pt^{4+}, respectively. The metallic Pt contribution was fitted using an asymmetric peak shape, which is essential for accurately describing the photoemission process of metallic Pt 4f and hence for reliably quantifying the oxidized species. The asymmetric tail was modeled based on parameters obtained from the Pt 4f spectrum of a sputter-cleaned Pt(111) reference sample. The binding energy of Pt^{2+} 4f$_{7/2}$ peak is consistent with the presence of Pt(OH)$_2$, while the Pt^{4+} is more likely associated to PtO$_2$.[60] For a good fitting all samples required a further peak, labelled as Pt$^{\delta+}$, located at *circa* +0.5–0.7 eV from the Pt^0 peak. A review of the literature reveals that this component, typically observed at +0.5–1.0 eV relative to the Pt^0 peak, has been previously identified in both *in situ* and *ex situ* XPS studies.[61–66] This shift is commonly attributed to chemical interactions between platinum and chemisorbed species, primarily carbon- and oxygen-containing groups as well as sub-stochiometric oxides and Pt-oxide clusters. Metallic Pt^0 was the predominant species across all samples (Table S1 and Fig. 4c). A correlation emerged between the specific surface area of the Pt crystallite and metallic platinum amount. Samples presenting lower SSA, thus larger nanoparticles, (PtGdO$_x$1-600, PtGdO$_x$1-600A, PtGdO$_x$1-360, and PtGdO$_x$1-360A, Table 3 and Table S1) exhibited similar and the highest concentrations of Pt^0. Conversely, samples with smaller SSA (PtGdO$_x$2-500 and PtGdO$_x$2-500A) displayed the lowest metallic platinum content, indicating greater surface oxidation. Samples PtGdO$_x$3-400 and PtGdO$_x$3-400A, which featured more broadly distributed nanoparticle sizes, showed intermediate levels of Pt^0 content. Notably, acid treatment consistently led to a slight reduction in the relative amount of Pt^0, accompanied by an increase in the concentration of oxidized Pt species.

XPS reveals the presence of Gadolinium in all the untreated samples (Fig. 4b). The Gd 4d doublet is characterized by a large FWHM. As van der Laan and co-authors have shown,[67,68] this phenomenon arises from multiplet splitting caused by the interaction between the 4d core hole and the 4f electrons, leading to the formation of ^{9}D and ^{7}D final ionic states. The peak centered at 143.0 eV corresponds to ^{9}D final state and was deconvoluted into five components (Fig. 4f and Figures S4a–c), each associated with total angular momentum quantum numbers $\bar{J}$ = 6, 5, 4, 3, 2, respectively (where $\bar{J}$ is related to the 4d–4f coupling as previously described[67]). Considering the fitting results for samples PtGdO$_x$1-600, PtGdO$_x$2-500 and PtGdO$_x$3-400, the binding energies of these components—141.8 (±0.1) eV, 142.8 (±0.1) eV, 143.9 (±0.1) eV, 144.8 (±0.1) eV and 145.7 (±0.1) eV—are in very good agreement with the values reported by Gupta *et al.*[33] for a Gd$_2$O$_3$ thin film on Si. This confirms that Gd is always present in the form of Gd$_2$O$_3$. The peak centered at 148.7 (±0.1) eV corresponds to the ^{7}D final state and was fitted by a single peak.

3.5 Electrochemical characterization

The PtGdO$_x$ catalysts were electrochemically characterized before and after acid treatment to assess the impact of the treatment on catalytic activity toward the oxygen reduction reaction and compare these findings with morphological

Table 3 Electrochemical data obtained from cyclic voltammetry and liner sweep voltammetry with RDE at 20 mV s^{-1} and 1600 rpm in O_2-saturated 0.1 M $HClO_4$

Samples	Gd salts	ECA $m^2\ g^{-1}$	$E_{1/2}$ V *vs.* RHE	$\lvert j_{0.9V\ vs.\ RHE}\rvert$ mA cm^{-2}	MA A g^{-1}	SA mA cm^{-2}	SSA $m^2\ g^{-1}$
TEC10V50E		34 ± 3	0.867 ± 0.005	2.00 ± 0.06	(20 ± 1) × 10	0.27 ± 0.01	
$PtGdO_x$1-360	NoAcd $GdCl_3$	33 ± 4	0.81 ± 0.01	1.64 ± 0.07	(11 ± 2) × 10	0.22 ± 0.02	
$PtGdO_x$1-360A	Acd $GdCl_3$	36 ± 4	0.85 ± 0.02	2.6 ± 0.2	(18 ± 4) × 10	0.49 ± 0.05	
$PtGdO_x$1-600	NoAcd GdCl3	32 ± 9	0.847 ± 0.007	1.8 ± 0.1	(12 ± 1) × 10	0.36 ± 0.05	
$PtGdO_x$1-600A	Acd $GdCl_3$	46 ± 5	0.86 ± 0.01	2.2 ± 0.2	(14 ± 1) × 10	0.32 ± 0.03	46.9
$PtGdO_x$2-500	NoAcd $Gd(acac)_3$	49 ± 7	0.851 ± 0.005	2.7 ± 0.2	(18 ± 2) × 10	0.37 ± 0.04	
$PtGdO_x$2-500A	Acd $Gd(acac)_3$	51 ± 4	0.877 ± 0.006	3.5 ± 0.5	(23 ± 3) × 10	0.46 ± 0.07	151.7
$PtGdO_x$3-400	NoAcd $Gd(ac)_3$	38 ± 1	0.864 ± 0.001	2.6 ± 0.4	(12 ± 3) × 10	0.45 ± 0.02	
$PtGdO_x$3-400A	Acd $Gd(ac)_3$	26 ± 1	0.85 ± 0.01	1.7 ± 0.3	(17 ± 2) × 10	0.35 ± 0.07	128.7

characterizations. Electrochemical data for the $PtGdO_x$ catalysts are summarized in Table 3.

Fig. 5a shows cyclic voltammetry curves recorded at 50 mV s^{-1} in 0.1 M $HClO_4$ for the most active catalysts: $PtGdO_x$1-600A, $PtGdO_x$2-500A, and $PtGdO_x$3-400A. CV curves for the untreated and acid-treated samples are compared in Figures S2a and c. The CV profiles of the $PtGdO_x$ catalysts exhibit well-defined H_2 adsorption/desorption peaks and low capacitive currents, indicating high purity and electrochemical stability.

Among the tested samples, $PtGdO_x$2-500A, synthesized with $Gd(acac)_3$, exhibits the highest kinetic current, with a half-wave potential of $E_{1/2}$ = 0.877 ± 0.006 V *vs.* RHE. This is 15 mV higher than other synthesized samples and significantly exceeds the $E_{1/2}$ of the pristine material value (0.851 ± 0.008 V *vs.* RHE, Table 3). LSV comparisons of untreated and acid-treated samples across various synthesis temperatures are shown in Figure S2b and d.

The histogram in Fig. 5d highlights the improvement in electrochemical performance, in terms of mass activity and specific activity, after H_2SO_4 washing. This improvement is likely due to reduced NP size and removal of residual Gd. The highest-performing catalyst, $PtGdO_x$2-500A, synthesized at 500 °C with $Gd(acac)_3$, displayed the best catalytic activity due to its very small NPs.

The catalytic activity trends, expressed as $E_{1/2}$ and mass activity, after acid treatment are as follows: $PtGdO_x$2-500A (230A g^{-1}) > $PtGdO_x$3-400A (172 A g^{-1}) > $PtGdO_x$1-600A (174 A g^{-1}) ≈ $PtGdO_x$1-360A (176 A g^{-1}). However, specific activity follows a different trend after acid treatment. In fact, it decreases due to the overall increase of the electrochemical active area compared to the kinetic current: $PtGdO_x$1-360A (494 μA cm^{-2}) > $PtGdO_x$2-500A (456 μA cm^{-2}) > $PtGdO_x$3-400A (350 μA cm^{-2}) > $PtGdO_x$1-600A (316 μA cm^{-2}). Catalysts with uncontrolled NP size and low surface density exhibited the lowest activities and limiting current densities.

Correlating the trends observed before and after acid treatment, as well as comparisons across synthesis temperatures, proved challenging when relying solely on TEM. Unfortunately, the low statistical representation provided by transmission electron microscopy is insufficient to fully capture the complexity of platinum nanoparticles unless complemented by other techniques. To address this limitation, XRD analysis is proposed as a method to quantify the exposed platinum

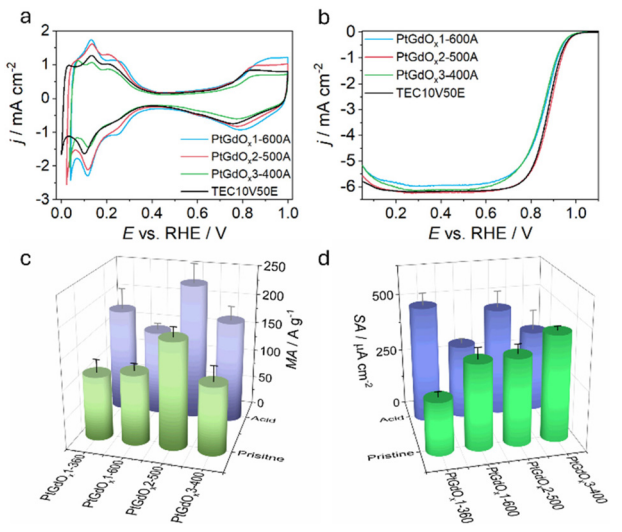

Fig. 5 (a) Cyclic voltammetry at 50 mV s^{-1} in Ar-saturated electrolyte; (b) LSV at RDE: v = 20 mV s^{-1} and ω = 1600 rpm in O_2 saturated 0.1 M $HClO_4$; (c and d) mass activity and specific activity extracted from RDE data at 20 mV s^{-1} and 1600 rpm.

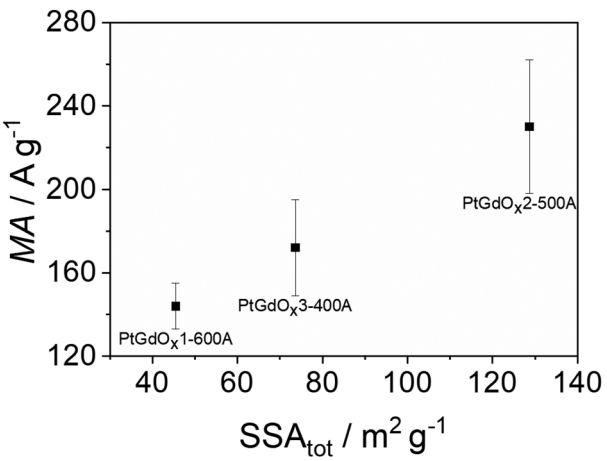

Fig. 6 Comparison between the specific activity and the specific surface area calculated with the DSE.

surface area, particularly for catalysts containing large platinum agglomerates. By interpreting the XRD spectra using the DSE, it becomes possible to calculate the specific surface area of the platinum nanoparticles. This approach also allows for the identification of unusual structural features, such as stacking faults or porosity, which may otherwise go unnoticed.

As shown in Fig. 6 and Table 3, a clear correlation is observed between the specific catalytic activity and the calculated SSA. This provides a more statistically robust method for linking catalytic performance to morphological characteristics. The findings highlight the significance of the WAXTS-DSE analysis for evaluating catalysts with variable size distributions, reinforcing its importance in accurately assessing the real efficiency of the catalysts.

4 Conclusions

This study investigates the effect of different gadolinium precursors on the nucleation and growth of Pt–carbon catalysts, demonstrating that the size of the resulting Pt nanoparticles is strongly influenced by the choice of precursor. XPS analysis confirmed the formation of Gd_2O_3, which was completely removed during the acid activation process to enhance the Pt active surface area. The two precursors, $Gd(acac)_3{\cdot}xH_2O$ and $Gd(ac)_3{\cdot}xH_2O$, drive the formation of smaller Pt nanoparticles, highlighting the potential of employing different Gd compounds to tailor the catalyst nanostructure and enhance its performance. Through WAXTS characterization and DSE analysis, it was possible to unravel the complex structure of the samples by calculating a specific parameter, SSA_{tot}, which accounts for all the Pt phases present. This surface-sensitive parameter showed a strong correlation with the catalytic activity of the samples toward the ORR. On the other hand, no residual strain effect was evidenced by DSE analysis after the Gd_2O_3 leaching.

Among the various catalyst morphologies, the $PtGdO_x$2-500A sample, synthesized using $Pt(acac)_2$ and $Gd(acac)_3$, and subjected to acid treatment, exhibited the highest ORR activity in a conventional electrochemical cell.

Author contributions

Mattia Parnigotto and Gregorio Dal Sasso, data acquisition, formal analysis and writing original draft; Marco Mazzucato data acquisition and revision; Maria Chiara Dalconi, Denis Badocco, Marzio Rancan, Paolo Pastore, Lidia Armelao and Enzo Menna data acquisition and formal analysis, Christian Durante, conceptualization, review & editing, supervision, visualization, methodology, funding acquisition.

Conflicts of interest

The authors declare that they have no known competing financial interests or personal relationships that could have appeared to influence the work reported in this paper.

Data availability

Supplementary information is available. See DOI: https://doi.org/10.1039/d5nr04642d.

Additional information is available from the corresponding authors upon reasonable request.

Acknowledgements

We gratefully acknowledge the University of Padova (Italy) and the Department of Chemical Sciences for their financial support. M. P. acknowledges PON "Ricerca e Innovazione" 2014–2020 for the PhD fellowship support. MIUR is also acknowledged for the support to the project financed by the European Union – Next Generation EU – Bando PRIN 2022 PNRR – M4.C2.1.1: Progetto: P2022WANKS – ECHO-EF. The ESCALAB QXi spectrometer was funded by the Italian National Research Council *via* the grant: "Sviluppo delle infrastrutture e programma biennale degli interventi del Consiglio Nazionale delle Ricerche (2019)". We acknowledge the scientific and technical staff at the X04SA-MS beamline of the Swiss Light Source (Paul Scherrer Institut, Villigen, CH) and for provision of synchrotron radiation beamtime under the proposal ID: 20211867.

References

1 J. Speder, A. Zana, I. Spanos, J. J. K. Kirkensgaard, K. Mortensen, M. Hanzlik and M. Arenz, *J. Power Sources*, 2014, **261**, 14–22.
2 A. A. Gewirth and M. S. Thorum, *Inorg. Chem.*, 2010, **49**, 3557–3566.
3 L. Su, W. Jia, C.-M. Li and Y. Lei, *ChemSusChem*, 2014, **7**, 361–378.
4 Y. Bing, H. Liu, L. Zhang, D. Ghosh and J. Zhang, *Chem. Soc. Rev.*, 2010, **39**, 2184.
5 G. Daniel, E. Foltran, R. Brandiele, L. Nodari, R. Pilot, E. Menna, G. A. Rizzi, A. A. Isse, C. Durante and A. Gennaro, *J. Power Sources*, 2018, **402**, 434–446.
6 G. Daniel, M. Mazzucato, R. Brandiele, L. De Lazzari, D. Badocco, P. Pastore, T. Kosmala, G. Granozzi and C. Durante, *ACS Appl. Mater. Interfaces*, 2021, **13**, 42693–42705.
7 M. Mazzucato and C. Durante, *Electrochim. Acta*, 2021, **394**, 139105.
8 I. Roche, E. Chaînet, M. Chatenet and J. Vondrák, *J. Phys. Chem. C*, 2007, **111**, 1434–1443.
9 S. Zhou, W. Liao, Z. Wang, M. Chen, J. Long, Q. Zhou and Q. Wang, *ACS Appl. Energy Mater.*, 2022, **5**, 6472–6480.
10 A. Gunnarson, J. De Bellis, T. Imhof, N. Pfänder, M. Ledendecker and F. Schüth, *Chem. Mater.*, 2023, **35**, 2006–2015.
11 S. Polani, R. Amitrano, A. F. Baumunk, L. Pan, J. Lu, N. Schmitt, U. Gernert, M. Klingenhof, S. Selve,

C. M. Günther, B. J. M. Etzold and P. Strasser, *ACS Appl. Mater. Interfaces*, 2024, **16**, 28.
12 H. Wang, J. Liu, K. Du, X. Wang, X. Li, Y. Liu, C. Min, F. Liu and X. Yang, *J. Power Sources*, 2024, **616**, 235127.
13 P. Hernandez-Fernandez, F. Masini, D. N. McCarthy, C. E. Strebel, D. Friebel, D. Deiana, P. Malacrida, A. Nierhoff, A. Bodin, A. M. Wise, J. H. Nielsen, T. W. Hansen, A. Nilsson, I. E. L. Stephens and I. Chorkendorff, *Nat. Chem.*, 2014, **6**, 732–738.
14 E. Antolini, J. R. C. Salgado, M. J. Giz and E. R. Gonzalez, *Int. J. Hydrogen Energy*, 2005, **30**, 1213–1220.
15 J. H. Kim, S. Chang and Y. T. Kim, *Appl. Catal., B*, 2014, **158–159**, 112–118.
16 M. P. Hyman and J. W. Medlin, *J. Phys. Chem. C*, 2007, **111**, 17052–17060.
17 R. Zhang, J. Sun, Y. Chen, Q. Shen, C. Ding, S. Zhang and J. Zhang, *Coord. Chem. Rev.*, 2025, **543**, 216958.
18 Y. Chen, Z. Jin, J. Sun, S. Chen, J. Zhang and S. Zhang, *eScience*, 2025, **5**, 100396.
19 R. Brandiele, V. Amendola, A. Guadagnini, G. A. Rizzi, D. Badocco, P. Pastore, A. A. Isse, C. Durante and A. Gennaro, *Electrochim. Acta*, 2019, **320**, 134563–134572.
20 R. Brandiele, A. Guadagnini, M. Parnigotto, F. Pini, V. Coviello, D. Badocco, P. Pastore, G. A. Rizzi, A. Vittadini, D. Forrer, V. Amendola and C. Durante, *J. Energy Chem.*, 2024, **92**, 508–520.
21 R. Brandiele, A. Guadagnini, L. Girardi, G. Dražić, M. C. Dalconi, G. A. Rizzi, V. Amendola and C. Durante, *Catal. Sci. Technol.*, 2020, **10**, 4503–4508.
22 R. Brandiele, C. Durante, E. Grądzka, G. A. Rizzi, J. Zheng, D. Badocco, P. Centomo, P. Pastore, G. Granozzi and A. Gennaro, *J. Mater. Chem. A*, 2016, **4**, 12232–12240.
23 R. Sandström, E. Gracia-Espino, G. Hu, A. Shchukarev, J. Ma and T. Wågberg, *Nano Energy*, 2018, **46**, 141–149.
24 C. A. Campos-Roldán, F. Pailloux, P. Y. Blanchard, D. J. Jones, J. Rozière and S. Cavaliere, *ACS Catal.*, 2021, **11**, 13519–13529.
25 A. Velázquez-Palenzuela, F. Masini, A. F. Pedersen, M. Escudero-Escribano, D. Deiana, P. Malacrida, T. W. Hansen, D. Friebel, A. Nilsson, I. E. L. Stephens and I. Chorkendorff, *J. Catal.*, 2015, **328**, 297–307.
26 C. Kim, F. Dionigi, V. Beermann, X. Wang, T. Möller and P. Strasser, *Adv. Mater.*, 2019, **31**, 1–19.
27 F. Ando, T. Gunji, T. Tanabe, I. Fukano, H. D. Abruña, J. Wu, T. Ohsaka and F. Matsumoto, *ACS Catal.*, 2021, **11**, 9317–9332.
28 S. G. Peera, T. G. Lee and A. K. Sahu, *Sustainable Energy Fuels*, 2019, **3**, 1866–1891.
29 Y. Luo, A. Habrioux, L. Calvillo, G. Granozzi and N. Alonso-Vante, *ChemCatChem*, 2015, **7**, 1573–1582.
30 P. Debye, *Ann. Phys.*, 1915, **351**, 809–823.
31 A. Cervellino, R. Frison, F. Bertolotti and A. Guagliardi, *J. Appl. Crystallogr.*, 2015, **48**, 2026–2032.
32 R. Brandiele, M. Parnigotto, M. Mazzucato, M. C. Dalconi, F. Bertolotti, G. A. Rizzi, G. D. Sasso and C. Durante, *Appl. Catal., B*, 2024, **344**, 123620.
33 J. A. Gupta, D. Landheer, G. I. Sproule, J. P. McCaffrey, M. J. Graham, K. C. Yang, Z. H. Lu and W. N. Lennard, *Appl. Surf. Sci.*, 2001, **173**, 318–326.
34 C. Zhang, S. Y. Hwang, A. Trout and Z. Peng, *J. Am. Chem. Soc.*, 2014, **136**, 7805–7808.
35 R. Brandiele, M. Zerbetto, M. C. Dalconi, G. A. Rizzi, A. A. Isse, C. Durante and A. Gennaro, *ChemSusChem*, 2019, **12**, 4229–4239.
36 K. Shinozaki, J. W. Zack, R. M. Richards, B. S. Pivovar and S. S. Kocha, *J. Electrochem. Soc.*, 2015, **162**, F1144.
37 H. A. Gasteiger, S. S. Kocha, B. Sompalli and F. T. Wagner, *Appl. Catal., B*, 2005, **56**, 9–35.
38 K. Shinozaki, J. W. Zack, S. Pylypenko, B. S. Pivovar and S. S. Kocha, *J. Electrochem. Soc.*, 2015, **162**, F1384–F1396.
39 O. A. Baturina, K. E. Swider-lyons, Y. Garsany and S. S. Kocha, *Anal. Chem.*, 2010, **82**, 6321–6328.
40 P. R. Willmott, D. Meister, S. J. Leake, M. Lange, A. Bergamaschi, M. Böge, M. Calvi, C. Cancellieri, N. Casati, A. Cervellino, Q. Chen, C. David, U. Flechsig, F. Gozzo, B. Henrich, S. Jäggi-Spielmann, B. Jakob, I. Kalichava, P. Karvinen, J. Krempasky, A. Lüdeke, R. Lüscher, S. Maag, C. Quitmann, M. L. Reinle-Schmitt, T. Schmidt, B. Schmitt, A. Streun, I. Vartiainen, M. Vitins, X. Wang and R. Wullschleger, *J. Synchrotron Radiat.*, 2013, **20**, 667–682.
41 F. Ferri, M. C. Bossuto, P. Anzini, A. Cervellino, A. Guagliardi, F. Bertolotti and N. Masciocchi, *Acta Crystallogr., Sect. A: Found. Adv.*, 2023, **79**, 587–596.
42 A. Cervellino, C. Giannini and A. Guagliardi, *J. Appl. Cryst.*, 2010, **43**, 1543–1547.
43 A. Cervellino, C. Giannini and A. Guagliardi, *J. Comput. Chem.*, 2006, **27**, 995–1008.
44 M. W. Terban and S. J. L. Billinge, *Chem. Rev.*, 2022, **122**, 1208–1272.
45 P. Juhás, T. Davis, C. L. Farrow and S. J. L. Billinge, *J. Appl. Crystallogr.*, 2013, **46**, 560–566.
46 F. Bertolotti, D. Moscheni, A. Migliori, S. Zacchini, A. Cervellino, A. Guagliardi and N. Masciocchi, *Acta Crystallogr., Sect. A: Found. Adv.*, 2016, **72**, 632–644.
47 B. Jankoviç and S. Mentus, *Metall. Mater. Trans. A*, 2009, **40**, 609–624.
48 C. Jackson, G. T. Smith, N. Mpofu, J. M. S. Dawson, T. Khoza, C. September, S. M. Taylor, D. W. Inwood, A. S. Leach, D. Kramer, A. E. Russell, A. R. J. Kucernak and P. B. J. Levecque, *RSC Adv.*, 2020, **10**, 19982–19996.
49 N. K. Sahu, A. Prakash and D. Bahadur, *Dalton Trans.*, 2014, **43**, 4892–4900.
50 I. V. Korzun, I. D. Zakir'yanova and E. V. Nikolaeva, *Russ. Metall.*, 2018, **2018**, 722–727.
51 V. P. Glibin, M. Cherif, F. Vidal, J.-P. Dodelet, G. Zhang and S. Sun, *J. Electrochem. Soc.*, 2019, **166**, F3277–F3286.
52 O. A. Baturina, S. R. Aubuchon and K. J. Wynne, *Chem. Mater.*, 2006, **18**, 1498–1504.
53 B. M. Abu-Zied, L. Obalová, K. Pacultová, K. Karásková, M. S. Al-Fakeh, A. M. Asiri and F. M. Alminderej, *Ceram Interfaces*, 2020, **46**, 25467–25477.

54 R. M. Mahfouz, M. A. S. Monshi and N. M. Abd El-Salam, *Thermochim. Acta*, 2002, **383**, 95–101.
55 F. Lv, Y. Zhang, X. Chen and Y. Ma, *Int. J. Opt. Photonic Eng.*, 2017, **2**, 1–8.
56 T. Y. Yoo, J. M. Yoo, A. K. Sinha, M. S. Bootharaju, E. Jung, H. S. Lee, B. H. Lee, J. Kim, W. H. Antink, Y. M. Kim, J. Lee, E. Lee, D. W. Lee, S. P. Cho, S. J. Yoo, Y. E. Sung and T. Hyeon, *J. Am. Chem. Soc.*, 2020, **142**, 14190–14200.
57 M. Parnigotto, G. Dal Sasso, E. Berretti, M. Mazzucato, F. Bertolotti, A. Lavacchi, M. C. Dalconi, L. Gavioli and C. Durante, *Small*, 2025, 2403127.
58 S. K. Ignatov, A. G. Razuvaev, A. S. Loginova and A. E. Masunov, *J. Phys. Chem. C*, 2019, **123**, 29024–29036.
59 B. C. Han, C. R. Miranda and G. Ceder, *Phys. Rev. B: Condens. Matter Mater. Phys.*, 2008, **77**, 075410.
60 A. Y. Lee, C. J. Powell, J. M. Gorham, A. Morey, J. H. J. Scott and R. J. Hanisch, *Data Sci. J.*, 2024, **23**, 1–9.
61 K. S. Kim, N. Winograd and R. E. Davis, *J. Am. Chem. Soc.*, 1971, **93**, 6296–6297.
62 O. Björneholm, A. Nilsson, H. Tillborg, P. Bennich, A. Sandell, B. Hernnäs, C. Puglia and N. Mårtensson, *Surf. Sci.*, 1994, **315**, L983–L989.
63 V. A. Saveleva, V. Papaefthimiou, M. K. Daletou, W. H. Doh, C. Ulhaq-Bouillet, M. Diebold, S. Zafeiratos and E. R. Savinova, *J. Phys. Chem. C*, 2016, **120**, 15930–15940.
64 R. Brown, M. Vorokhta, T. Skála, I. Khalakhan, N. Lindahl, B. Eriksson, C. Lagergren, I. Matolínová, V. Matolín and B. Wickman, *Fuel Cells*, 2020, **20**, 413–419.
65 C. C. Yang, M. H. Tsai, Z. R. Yang, Y. C. Tseng and C. H. Wang, *ChemCatChem*, 2023, **15**, e202300359.
66 G. Held, L. B. Jones, E. A. Seddon and D. A. King, *J. Phys. Chem. B*, 2005, **109**, 6159–6163.
67 G. van der Laan, E. Arenholz, E. Navas, A. Bauer and G. Kaindl, *Phys. Rev. B: Condens. Matter Mater. Phys.*, 1996, **53**, R5998.
68 W. Lademan, A. See, L. Klebanoff and G. van der Laan, *Phys. Rev. B: Condens. Matter Mater. Phys.*, 1996, **54**, 17191.